Displacement hazard from distributed ruptures in strike-slip earthquakes

Alba M. Rodriguez Padilla *[1] and Michael E. Oskin[1]

[1] *Department of Earth and Planetary Sciences, University of California, Davis*

Abstract

Widespread distributed fracturing during earthquakes threatens infrastructure and lifelines. We combine high-resolution rupture maps from the five major surface-rupturing strike-slip earthquakes in southern California and northern Mexico since 1992 to incorporate the displacements produced by distributed ruptures into a probabilistic displacement hazard analysis framework. Through analysis of the spatial distribution of mapped ruptures and displacements for each of these events, we develop a magnitude-dependent expression for the probability per unit area of finding a distributed rupture that accommodates a displacement that exceeds a displacement threshold at a given distance away from the principal fault. Our model is best applied to estimating expected distributed displacements for strike-slip earthquakes, similar to those analyzed, with widespread ruptures across immature fault zones.

Key points

1. Strike-slip earthquakes on immature faults cause widespread ruptures that can threaten infrastructure.
2. We present a probabilistic fault displacement model based on rupture maps and displacement measurements.
3. Our model estimates distributed rupture displacement hazard for strike-slip events on immature faults.

Introduction

Displacements from surface-rupturing earthquakes directly threaten infrastructure and lifelines in tectonically active regions. Probabilistic fault displacement hazard analysis (PFDHA) addresses this challenge by providing estimates of the likelihood and distribution of surface displacements during fault rupture (e.g. Youngs et al., 2003; Petersen et al., 2011; Moss and Ross, 2011; Takao et al., 2013; Nurminen et al., 2020; Wang and Goulet, 2021; Scott et al., 2023). Over the past few years, earth scientists and engineers have joined efforts in generating standardized empirical databases to constrain fault displacement hazard models (Sarmiento et al., 2021; Nurminen et al., 2022).

*Corresponding author. arodriguezpadilla@ucdavis.edu

The data these efforts are based on has improved due to increased coverage of surface rupturing earthquakes (e.g. airborne lidar, Chen et al., 2015; Hudnut et al., 2020), better post-earthquake response coordination (e.g. Civico et al., 2018, Mattioli et al., 2020, Baize et al., 2022), and advances in the repeat frequency and resolution of geodetic methods (e.g. Milliner and Donnellan, 2020; Xu et al., 2020).

We present a fault displacement model focused on distributed ruptures for strike-slip faults using data from five major surface rupturing earthquakes in the Eastern California Shear Zone and Northern Mexico. These events left behind impressive footprints of broadly distributed ruptures in the desert that have been carefully mapped: the Landers (1992), Hector Mine (1999), El Mayor-Cucapah (2010), and Ridgecrest (2019 foreshock and mainshock) earthquakes (Sieh et al., 1993; Lazarte et al., 1994; Treiman et al., 2002; Hudnut et al., 2002; Fletcher et al., 2014; Teran et al., 2015; Milliner et al., 2015; Milliner et al., 2016; Ponti et al., 2020; DuRoss et al., 2020; Rodriguez Padilla et al., 2022a). The hazard posed by distributed ruptures remains poorly characterized for strike-slip earthquakes, challenging the ability of engineers and other stakeholders to evaluate the associated risk. In this contribution, we use surface rupture maps and displacement measurements from these well-documented earthquakes to help fill this data gap. To do so, we develop a relationship for the probability per unit area of finding a rupture at a distance away from the principal fault that will have a displacement greater than a threshold. This relationship may be used by end-users to quantify surface displacement hazard in a probabilistic framework that can inform the design and evaluation of lifelines and engineered structures located near or across active fault zones.

Surface rupture and displacement measurements

The Fault Displacement Hazard Initiative (FDHI) database, hosted and maintained by the Natural Hazards Risk & Resilience Research Center at the University of California, Los Angeles, includes 66 surface-rupturing earthquakes, with moment magnitudes ranging from 5.0 to 8.0, of all faulting styles (Sarmiento et al., 2021). The database incorporates surface rupture maps and displacement measurements for each of the events. The displacements are attributed with location, amount, and, sometimes, direction. The ruptures are classified as primary or secondary. For the strike-slip events considered in this study, ruptures occur in a continuum of decaying density (see methods section), without a distinct change from localized or primary to distributed or secondary, and thus we classify all ruptures in the FDHI database for these events as distributed for the purpose of our study.

We select five strike-slip events from the FDHI rupture database to incorporate into our model: the 1992 M_W7.3 Landers, 1999 M_W 7.1 Hector Mine, 2010 M_W 7.2 El Mayor-Cucapah, and 2019 Ridgecrest earthquakes (separated into M_w 6.4 foreshock and M_w 7.1 mainshock; Figure 1). We choose these events because they are well-mapped, occurred on relatively immature faults (<25 km cumulative displacement), and share the same regional tectonic setting (Eastern California Shear Zone and northern Baja California transtensional rift).

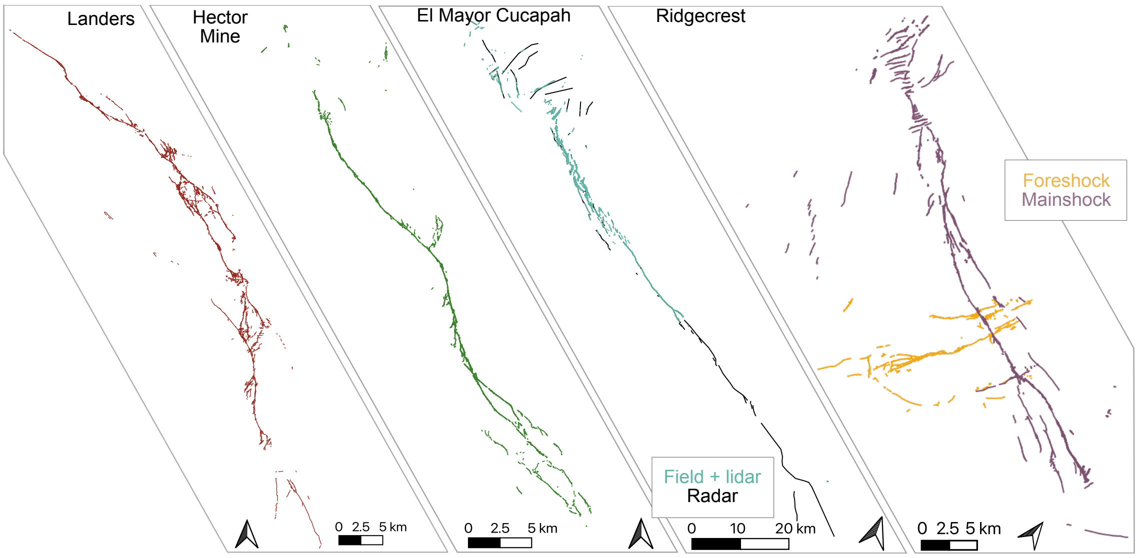

Figure 1: Surface rupture maps from the Landers, Hector Mine, El Mayor-Cucapah, and Ridgecrest earthquakes from the Fault Displacement Hazard Initiative (FDHI) database (Sarmiento et al., 2021). The black lines in the El Mayor-Cucapah rupture are simplified traces mapped from radar data and excluded in this study. The turquoise lines were mapped from field and lidar data and included here. The purple lines in the Ridgecrest map represent the mainshock rupture map and the orange lines represent the foreshock rupture map.

The surface rupture maps in the FDHI database include some variability in completeness and mapping style. Overall, the near-field region of these earthquakes (<1 km from the principal rupture trace) is mapped at a similar resolution, while the far-field has some variability in spatial completeness and resolution. Specifically, the rupture map for the El Mayor-Cucapah earthquake includes ruptures mapped from radar data at its northern end into southern California and its southern end through the Colorado River Delta (Figure 1)(Fletcher et al., 2014). These rupture traces are depicted more simply than the field- and lidar-based ruptures, and may introduce an unrealistic bias in the rupture population. Accordingly, we remove these radar-based rupture traces from our dataset. Similarly, the foreshock and mainshock Ridgecrest maps contain some ruptures that are doubly mapped, redundant from the original maps of Ponti et al. (2020) and DuRoss et al. (2020), which are both included in the FDHI database maps of the Ridgecrest events. When there are redundant features, we remove the simpler traces.

A displacement model for distributed ruptures from surface rupture and displacement maps

Our model estimates the probability per unit area of finding a rupture at a distance x away from the principal rupture with slip greater than a threshold S_0. Computing this probability requires knowledge of the spatial distribution of ruptures and the displacements that these ruptures could accommodate. We address the former through analysis of the distribution of rupture density and the latter by examining the distribution of surface displacements measured for each of our selected events. The distributed displacement hazard results from the joint probability,

$$P(S > S_0|x, M_W) = P(rupture|x)P(S > S_0|x, rupture, M_W), \quad (1)$$

where $P(S > S_0|x, M_\mathrm{w})$ is the probability per unit area of finding a rupture at a distance away from the fault, resulting from an event of a given magnitude, that will have a displacement greater than the threshold S_0. $P(rupture|x)$ is the probability of rupture per unit area occurring at that location of distance x from the principal rupture. $P(S > S_0|x, rupture, M_\mathrm{w})$ is the displacement exceedance, a probability of finding a displacement that exceeds that threshold at a given distance from the fault, given the presence of a rupture, for a given earthquake magnitude.

The probability of observing a rupture at a given distance away from the principal rupture (the first term in equation 1) can be estimated from the spatial distribution of fracture density (e.g. Rodriguez Padilla et al., 2022b), which is given by the inverse power-law:

$$\nu(x) = \nu_o \left(\frac{x + x_{fr}}{x_{fr}}\right)^{-\gamma} \quad (2)$$

Where ν_o is the rupture density at the origin in number of ruptures per unit $1m^2$ area and x_{fr} is a normalizing constant and related to the uncertainty of the location of the principal fault trace in meters (Rodriguez Padilla et al., 2022b). The exponent γ is the slope of the decay of rupture density with distance, for values of $x > d$ in log-log space, or scaling exponent. The probability of a rupture occurrence per unit $1m^2$ area is given by $\nu(x)$.

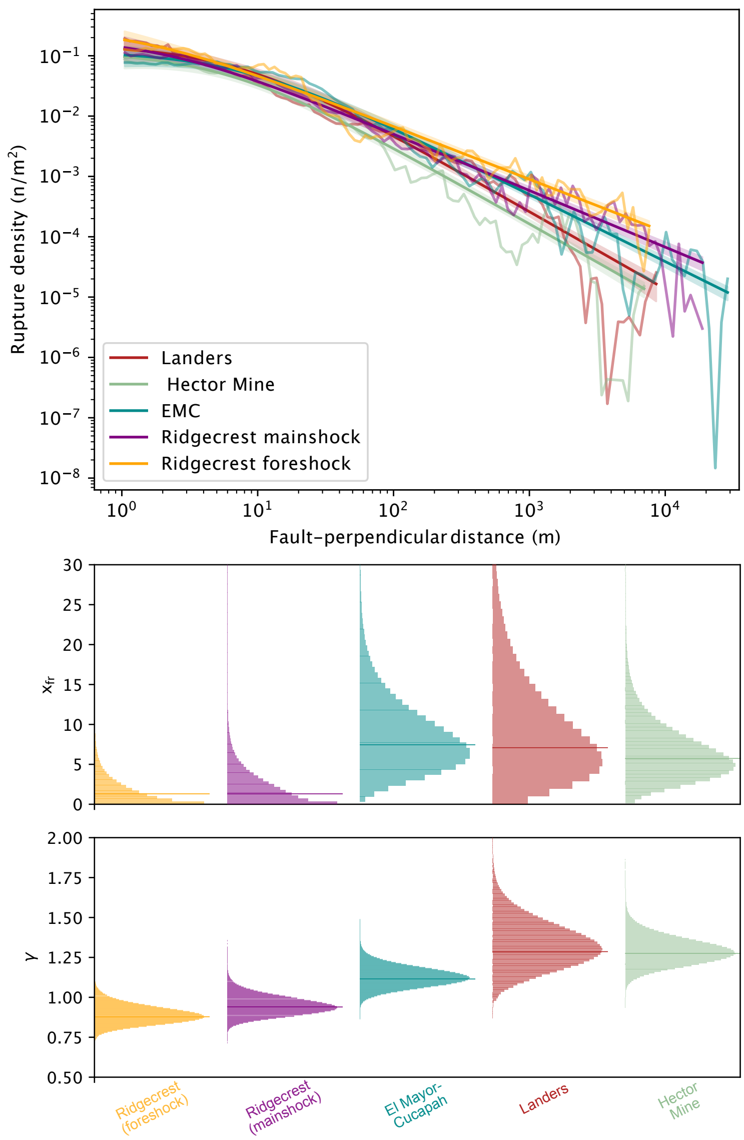

Figure 2: Rupture density distribution (i.e. the probability of finding a rupture per unit area) for the Landers, Hector Mine, El Mayor-Cucapah, and Ridgecrest earthquakes. The Ridgecrest foreshock and mainshock are shown as separate events. The shaded region represents the fits within one standard deviation of the maximum likelihood fit, shown as the bold line, fit using equation 2. The bottom graphs show the distribution of posterior values for x_{fr}, the uncertainty on the location of the principal fault trace, and for γ, the scaling exponent of the density-distribution.

We use equation 2 to calculate the rupture density distribution (and thus the probability of finding a rupture per unit area) for the Landers, Hector Mine, El Mayor-Cucapah, and Ridgecrest earthquakes based on the surface rupture maps for these events in the FDHI database (Figure 2). To do this, we discretize individual ruptures into 1-meter spaced points so that mapping choices do not bias the rupture density estimates (Rodriguez Padilla et al., 2022b). We measure the shortest distance between each discretized point and the principal rupture, without considering the azimuth of the point (i.e. whether points are ahead of a fault tip and parallel to the rupture, or they are along the rupture and therefore perpendicular to it). The principal rupture trace for each event (i.e. the fault with respect to which fault-perpendicular distance is measured) is simplified from the ruptures mapped as primary in each of the rupture maps in the FDHI rupture database (Figure 8 in the appendix), with the exception of the Ridgecrest mainshock where a second fault in the middle of the dry lake bed was added based on the mapping of Rodriguez Padilla et al. (2022b).

We fit each parameter in equation 2 to the rupture data using an ensemble sampler Monte Carlo Markov Chain (see supplementary methods section). The maximum likelihood fits and posterior distributions for x_{fr} and γ are shown in Figure 2 and provided in Table 1. Note that the rupture distributions appear to be independent of earthquake magnitude, with all events having similar rupture densities ν_o at the fault, hence the magnitude-independence of the first term in equation 1.

To assess displacement exceedance (second term in equation 1), we include only the displacements in the FDHI database (supplementary Figure 9) measured in the field, and exclude measurements derived from other techniques, such as image correlation. This is to ensure that the displacement measurements we consider are collected over apertures consistent with the width of individual ruptures. Among the field measurements, we select those labeled as "net preferred" for our models, as these are the measurements recommended for analysis by the FDHI database authors. The vast majority of the displacements in the database are lateral and therefore record shear, with a minor portion of them recorded in absolute terms, where multiple directional components are recorded as a ratio, representing a mixed-mode fracture. Because of the limited information available on fracture mode and displacement direction, our models are constructed without consideration of these parameters.

Coseismic displacements are highest along the principal rupture trace and decline to lower values on more distant distributed ruptures. We find that the mean values of displacement measurements from the FDHI database, binned with respect to distance to the principal fault trace, may be modeled as an inverse power-law described by:

$$\lambda(x) = \beta \left(\frac{x + x_S}{x_S} \right)^{-n} \tag{3}$$

where λ is the mean of the displacement at every distance bin, β is the average displacement at the origin, x is the location away from the principal fault trace in meters, x_S is a normalization factor held constant at 1 meter (see supplementary methods in the appendix), and n is the slope of the relationship between mean displacement and distance in log-log space, or the scaling exponent.

We fit equation 3 to the distribution of average displacements with distance for each of the events using an ensemble sampler for Monte-Carlo Markov Chain (see appendix for detailed method). The maximum likelihood fits and posterior distributions for β and n are shown in Figure 3 and provided in Table 1. Values of β range from 1 meter for the Ridgecrest foreshock to 4.2 meters for the Hector Mine event, broadly consistent with the average slip at the fault in each earthquake.

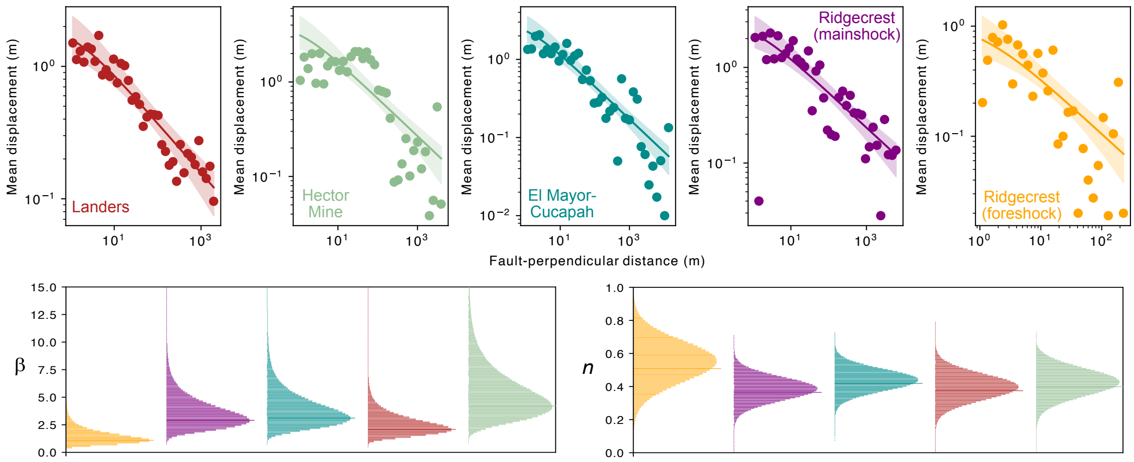

Figure 3: Distribution of average displacement measured in the field for the Landers, Hector Mine, El Mayor-Cucapah, and Ridgecrest earthquakes. The scattered dots on the top plot represent the field displacement data for each event from the FDHI database (Sarmiento et al., 2021). The solid lines represent the maximum likelihood fits to the distribution and the shaded area shows the 1σ posterior distribution from a Markov Chain Monte Carlo fit. The bottom panels show the posterior distributions of β and n, fit using equation 3.

We find that the values of n agree between the different events, averaging around 0.4, though the fits of equation 3 to the displacements vary in quality between events, with the Ridgecrest foreshock and the Hector Mine events being not well characterized by the power-law decay in equation 3. This poor characterization arises from the broader zone of similar average displacement measurements near the principal fault trace, and much higher scatter in the further (< 1 km from the fault in Hector Mine and < 100 m from the fault in the Ridgecrest foreshock) displacements measured in the field (Figure 3). This is clear in the residuals of the fit of equation 3 to the field displacement data from these two events (Figure 10 in the appendix). In the case of the Ridgecrest foreshock, the constant average displacement values near the principal fault may arise from incomplete rupture to the surface, which may be a magnitude-dependent characteristic. This is something we do not address in our model. The spatial distribution of mean displacement is well described by equation 3 for the Ridgecrest mainshock, the Landers, and the El Mayor-Cucapah events, as shown by the generally low residuals (<20% of β) of the fit of equation 3 to the field displacement data (figure 10 in the appendix).

Within each distance bin (see supplementary methods for details), we find that the population of field displacement measurements can be described by exponential or log-normal distributions (Figure 4). Both the exponential and log-normal models fit the data comparatively well for the range of observed slip values near the fault (Figure 4) for the Ridgecrest mainshock, the Ridgecrest foreshock, the Landers, and the Hector Mine events. The El Mayor-Cucapah ECDF is best described by the uniform CDF, though none of the distributions tested describe the data exceptionally well. For all events, beyond the range of observable displacements, the log-normal and exponential distributions would make different predictions that would result in slightly different probabilistic models in the latter steps in this method. Without observational data spanning higher slip values, we prefer the simpler form and less heavy-tailed behavior of the exponential relationship.

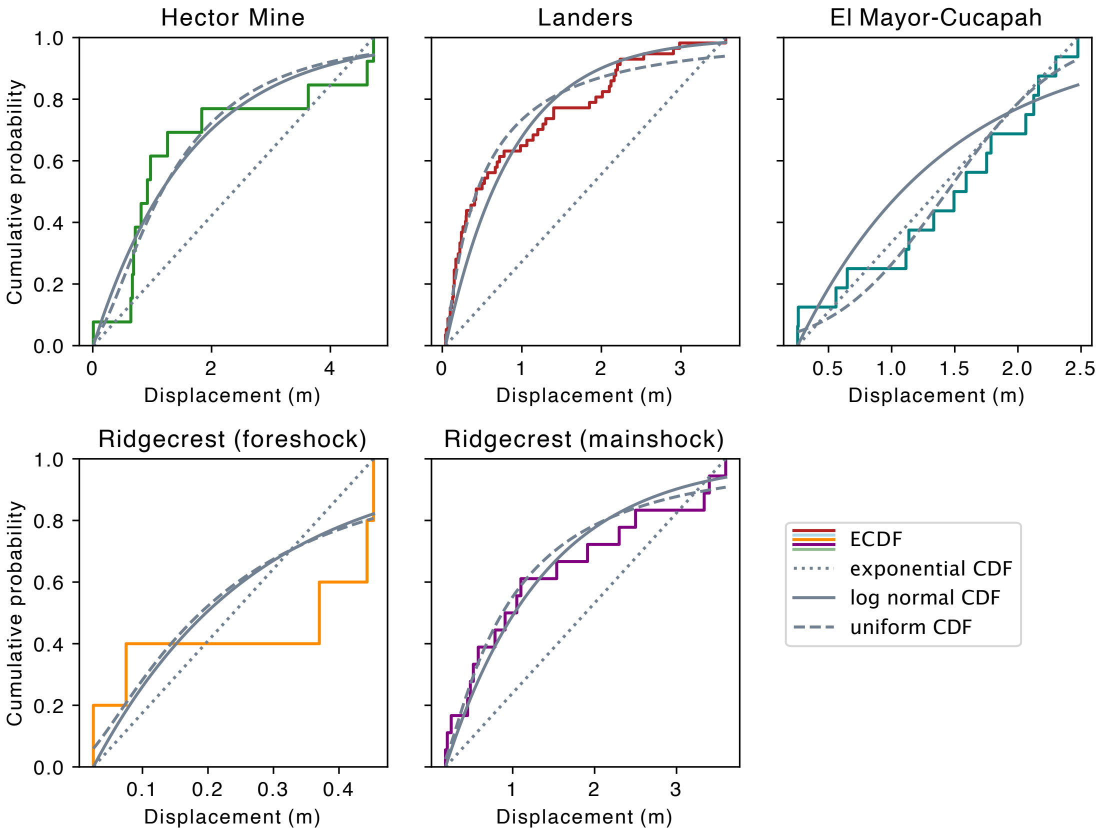

Figure 4: Empirical cumulative distribution functions (ECDF) of the displacements within 6-8 meters away from the fault for the Landers, Hector Mine, El Mayor-Cucapah, and Ridgecrest earthquakes. The cumulative distribution functions fit for exponential, log-normal, and uniform distributions are shown on top.

This exponential relationship holds up well for all of the distance bins analyzed, as shown by the observation of similar values for the mean and the standard deviation of displacement measurements within each bin (supplementary figure 11). The distribution of displacements within a distance bin can thus be described as follows:

$$f(S|x) = \frac{1}{\lambda} e^{\frac{-S}{\lambda}} \tag{4}$$

where λ, the mean of the displacement at every distance bin, is the output of equation 3. Combining equations 3 and 4 yields:

$$f(S) = \frac{1}{\beta} \left(\frac{x + x_S}{x_S} \right)^n e^{-\frac{S}{\beta} \left(\frac{x + x_S}{x_S} \right)^n} \tag{5}$$

Equation 5 is a probability density function (PDF) of observed displacements with distance from the principal fault trace. We integrate this PDF from S_0, the threshold displacement of interest, to S_{max}, the maximum observed slip in an event (note that we expect $S_{max} \geq \beta$), to solve for the probability of observing a displacement that exceeds S_0 on an observed rupture given an earthquake magnitude (second term of equation 1):

$$\begin{aligned} P(S > S_0|x, rupture, M_W) &= \int_{S_0}^{S_{max}} \frac{1}{\beta} \left(\frac{x + x_S}{x_S} \right)^n \\ &\qquad e^{-\frac{S}{\beta}(\frac{x+x_S}{x_S})^n} dS \\ &= -e^{-\frac{S}{\beta}(\frac{x+x_S}{x_S})^n} \Big|_{S_0}^{S_{max}} \end{aligned} \tag{6}$$

Note that in evaluating this integral, the term containing S_{max} is small, so that as long as $S_0 << S_{max}$, this term can be ignored. This limits the appropriate application of our model to predicting the probability of distributed displacements above a threshold that is a fraction (i.e. 10%) of the slip measured on the primary fault trace. This limitation is appropriate because solving only for the probability of large slip values would be akin to predicting the presence of another primary fault trace, which is not the objective of this model. With this application in mind, completing the integration of equation 6 yields:

$$P(S > S_0|x, rupture, M_W) = e^{\frac{-S_0}{\beta}(\frac{x+x_S}{x_S})^n} \tag{7}$$

The displacement threshold, S_0, may be adjusted by end-users for different engineering applications. Combining the probabilities in equations 2 and 7 yields the solution to equation 1:

$$P(S > S_0|x, M_W) = \nu_o \left(\frac{x + x_f}{x_f} \right)^{-\gamma} e^{\frac{-S_0}{\beta}\left(\frac{x+x_S}{x_S}\right)^n} \tag{8}$$

Note that the magnitude-dependence in this model arises from parameter β, the average displacement on the fault.

Figure 5 shows the relationship in equation 8 for each dataset for x= 1 to x=10 kilometers away from the fault, consistent with the extent of ruptures shown in Figure 2, with example values of S_0 of 0.01, 0.1, and 0.5 meters. The probabilities of finding a rupture that hosts displacements larger than 1 cm near the fault exceed 10% for all of the events considered here, reaching 20% for the Ridgecrest foreshock (Figure 5, left). Despite the smaller magnitude, the Ridgecrest foreshock has the highest rupture density predicted at the fault, which results in higher probabilities $P(S > S_0)$, despite the lower value of β, at this displacement threshold. $P(S > S_0)$ decreases rapidly with distance for all events, even for this small value of S_0, such that the probability of finding a rupture that hosts a displacement larger than 1 cm is lower than 1 in 1,000 beyond 300 m-1 km from the primary fault trace depending on the event.

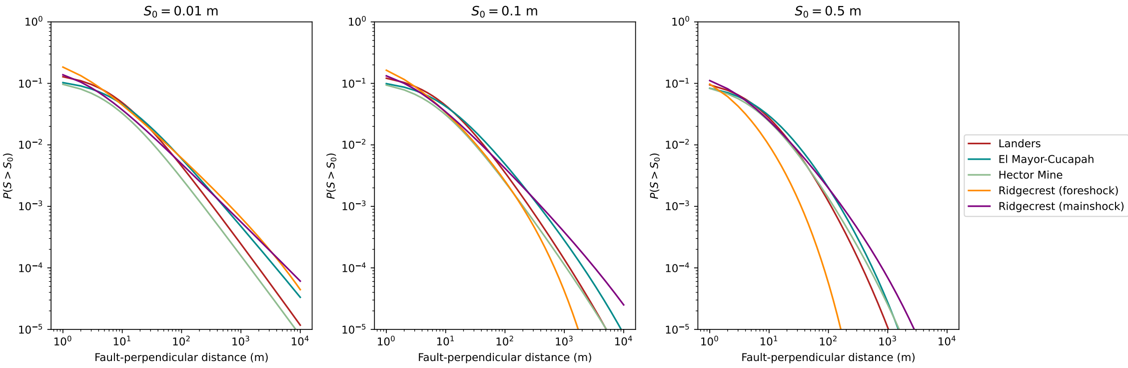

Figure 5: Curves showing the probability per square meter of finding a rupture hosting a displacement that exceeds threshold S_0 for the Landers, Hector Mine, El Mayor-Cucapah, and Ridgecrest earthquakes. The models are generated using equation 8. We show models for $S_0 = 0.01$ m, 0.1 m, and 0.5 m.

The surface rupture hazard curves for the Ridgecrest mainshock, Landers, El Mayor-Cucapah, and Hector Mine events look very similar for $S_0 = 1$ cm to those for $S_0 = 10$ cm. The variability of $P(S > S_0)$, about a factor of 2, at the intercept, arises largely from the variability in rupture density for the different events and likely reflects the natural variability that may be expected for these events and low displacement thresholds, regardless of magnitude (Figure 5, center). The magnitude-dependence of the model becomes clear with increasing distance away from the fault, given by the larger slope of $P(S > S_0)$ for the smaller-magnitude Ridgecrest foreshock. This pattern becomes even more obvious for the $P(S > S_0)$ curves where $S_0 = 0.5$ meters (Figure 5, right). At this displacement threshold, the effect of magnitude, captured by parameter β, trumps that of rupture density at the intercept and the Ridgecrest foreshock has a lower probability of finding a rupture hosting a displacement larger than 0.5 meters than that of the mainshock or Landers. When $S_0 = 0.5$ m, $P(S > S_0)$ becomes lower than 1 in 10,000 at about 500 m-1 km from the fault for the Ridgecrest mainshock, the Landers, the Hector Mine, and the El Mayor-Cucapah events. This hazard level is crossed at about 200 m from the fault for the Ridgecrest foreshock.

A generalized rupture-displacement probability model

e individual models of $P(S > S_0)$ for each event (Figure 5) can be used to inform a general model that is representative of events like these, i.e., those dominated by distributed deformation, largely rupturing through sediment, hosted on immature fault zones.

To estimate the first term of $P(S > S_0)$ for the general model, which is independent of earthquake magnitude, we combine the rupture distributions from the FDHI database from these five earthquakes and estimate a general relationship for rupture density with fault-perpendicular distance using equation 2 (figure 12 in the appendix). This is possible because the parameters describing the spatial distributions of rupture density for all events overlap within error, irrespective of magnitude or other event characteristics.

The second term in $P(S > S_0)$ is magnitude-dependent and therefore requires more careful examination to be generalized. The scaling exponent, n, that describes the spatial distribution of mean displacement is very consistent for the M_W 7.1 Ridgecrest mainshock, the M_W 7.3 Landers, and the M_W 7.2 El Mayor-Cucapah events, and the distribution of field displacements for these events is well described by equation 3, as captured by the low residuals (figure 10 in the appendix). Thus, to estimate n in our general model, we combine the posterior distributions of n from the Landers, El Mayor-Cucapah, and Ridgecrest mainshock displacement distributions (Figure 13 in the appendix). We find that n is normally distributed with a mean value of 0.41 and a standard deviation of 0.07.

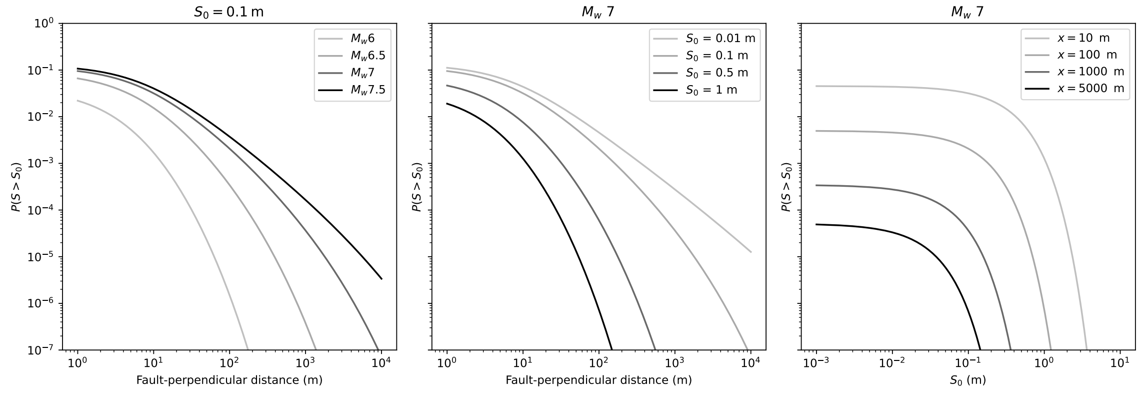

Figure 6: Curves showing the probability per square meter of finding a rupture hosting a displacement that exceeds threshold S_0 for a surface-rupturing strike-slip earthquake. The models are generated using equation 8. On the left, we show models for $M_W = 6$, 6.5, 7, and 7.5, where $S_0 = 0.1$ m. On the center, we show models for $S_0 = 0.01$, 0.1, 0.5, and 1 meter, for a M_W 7 event.On the right, we show probability ($P(S > S_0)$) versus displacement hazard curves for an M_W 7 event at distances of 10 m, 100 m, 1 km, and 5 km from the fault.

The magnitude-dependence of our probabilistic displacement model arises from parameter β, which we propose may be estimated using the empirical relationship for average displacement as a function of magnitude using the displacement measurements in the FDHI database:

$$log_{10}(\beta) = bM_W - a \tag{9}$$

where $a = 6.8701 \pm 0.2446$ and $b = 0.9629 \pm 0.1288$ are the regression coefficients and their respective standard errors, determined for strike-slip earthquakes in the regression in Figure 14 in the appendix. We rely on the displacements labeled as 'preferred' in the FDHI database to estimate the mean displacement for each strike-slip event. We are not able to use displacements measured in the field only because six of the strike-slip events in the database had displacements measured fully remotely. Two examples of the general model are shown in Figure 6. One for events of $M_W = 6$, 6.5, 7 and 7.5, all with $S_0 = 0.1$ m (Figure 6, left), and a second for values of $S_0 = 0.01$, 0.1, 0.5, and 1 m for an M_W 7 event (Figure 6, center). The magnitude dependence of $P(S > S_0)$ for a fixed displacement threshold S_0 manifests as an increasingly wider hazard envelope, i.e. slope decreases and intercept increases with increasing magnitude. For a fixed magnitude, the slope describing the probability $P(S > S_0)$ increases with increasing displacement threshold S_0, and the intercept decreases. The relationship of $P(S > S_0)$ and displacement threshold (Figure 6, right) shows an increasingly larger hazard envelope (i.e. larger probability for a given displacement threshold), for closer distances x to the fault.

Parameter uncertainty estimates

The parameters that build our probabilistic displacement model $P(S > S_0)$ have uncertainties that must be accounted for. The sources of uncertainty in the model are the fitting error in the exponent n that describes the PDF of displacements for an event, the uncertainty in the average displacement at the fault, β, and the uncertainty in the fits to x_{fr}, ν_o, and γ which describe the spatial distribution of rupture density.

To combine the errors in both terms in equation 8, we make a prediction for $P(S > S_0)$ under each set of samples from our suite of 5000 combined parameter sets. The parameters in the first term of equation 8, which describe the spatial distribution of rupture density, are correlated, so they must be sampled from the same state of the Markov chain for this correlation to be preserved (Figure 15 in the appendix). The parameters in the displacement term in equation 8 are normally distributed. To account for the variability of parameter n, we draw samples from a normal distribution with the mean and standard deviations reported in the previous section. The uncertainty of the average displacement β is given by the standard error of the regression that describes the scaling of mean displacement with magnitude. To account for the expected variability in β, we sample from a normal distribution where the mean is given by the best-fit value from our linear regression to the data in the FDHI database, and the standard error of the regression serves as the standard deviation of the distribution.

A general model with $S_0 = 0.1$ m and M_W 7, with uncertainties, as well as the model residuals resulting from the 5000 iterations of Monte Carlo sampling are shown in Figure 7. The incompleteness of the rupture maps in the far field contributes to the conical shape of the uncertainty distribution, which is largely inherited from the uncertainty in the rupture density and average displacement scaling exponents, γ and n. We estimate the one standard error by estimating the envelope of model fits at the 16^{th} and 84^{th} percentiles (1σ). Based on these envelopes, we expect variability in probability below one order of magnitude for $P(S > S_0)$ within 3 kilometers of the fault, increasing up to 6 orders of magnitude at 10 km away from the fault. The standard error can be described by the expression:

$$\sigma_M = \tau e^{x^{0.15}} \tag{10}$$

where $\tau \approx 5x10^{-2}$ for the 84% percentile and $\tau \approx -0.10$ for the 16% percentile. The fits of equation 10 to the model fits are shown in red in Figure 7.

We provide a Jupyter Notebook (see data and resources) that allows end-users to generate their own model for $P(S > S_0)$. The only inputs required are a displacement threshold S_0 and an earthquake moment magnitude (M_W). The model outputs $P(S > S_0)$ curves with a best-fit model and an analytically defined uncertainty range using equation 10.

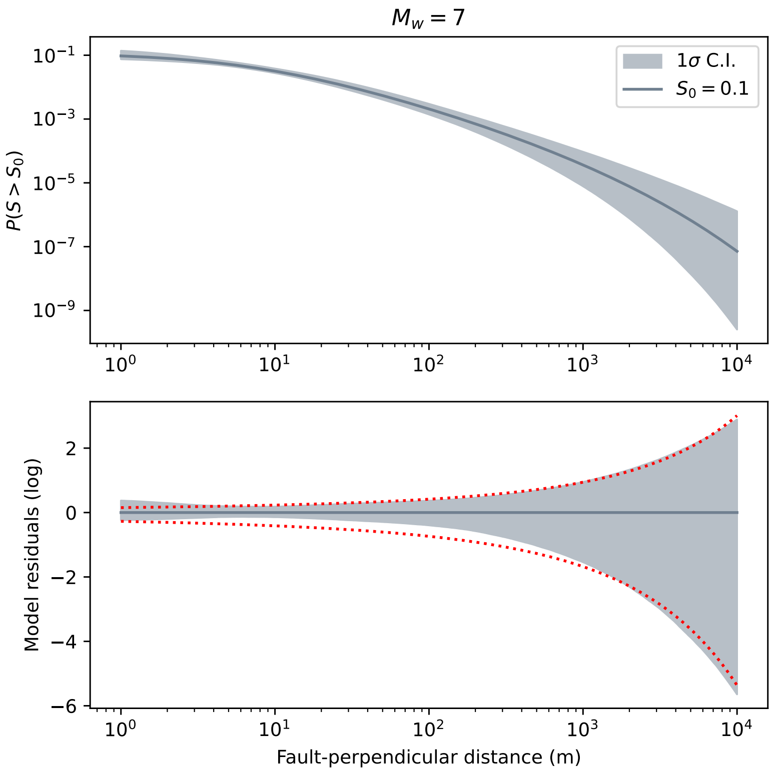

Figure 7: Top: PFDHA model expressing the probability of finding a rupture hosting a displacement that exceeds threshold $S_0 = 0.1$ m for a surface-rupturing strike-slip earthquake of M_W 7. The model is generated using equation 8. The shading represents the 1σ confidence intervals. The solid line represents the best-fit model. Bottom: Model residuals (log). The dotted red line represents the fit of equation 10 to the logarithm of the residuals. A version of this plot showing the 95% confidence intervals is shown in the appendix (Figure 17).

Model discussion and limitations

The model we develop in this contribution is based on rupture maps and field displacement measurements from select events in the Eastern California Shear Zone and northern Baja California. From our limited number of available surface rupturing events with high-resolution maps, there arise some challenges and assumptions in this model that limit its application.

Magnitude-dependence

Rupture density has no observable dependence on earthquake magnitude within the events studied, which span a range of magnitudes between M_W 6.4-7.3. However, this could change with an expanded dataset of high-resolution maps from more events. We find that, with the data available, the distributed rupture densities at the principal fault vary by less than a factor of 10, this is a level of variability accounted for in the model uncertainties discussed earlier. The rupture density variability documented by Rodriguez Padilla et al. (2022b) between different portions of the Ridgecrest 2019 surface ruptures, which they found to be independent of the displacement magnitude at the surface, exceeds this level of variability. Additionally, the ruptures we use as model inputs largely occurred through sediment, which may exert an important effect in rupture density. This is consistent with the work of Petersen et al. (2011), who found no dependence between the probability of observing a rupture off-fault and the magnitude of the event. Hence there is no basis at this time to develop a magnitude-dependent estimator of distributed rupture density.

It is reasonable to expect some association between the maximum distance from the fault at which ruptures are observed and earthquake magnitude, but no such relation can be derived from our study. The maximum distance observable is currently limited by the footprint available to map. Similarly, while the rupture tips tend to have more distributed ruptures extending away from them, the currently incomplete azimuthal coverage of ruptures precludes determining whether a higher frequency and extent of distributed ruptures at fault tips stem from a mapping bias or a physical feature (e.g. resulting from rupture directivity effects). Long-range azimuthal coverage for future events should enable assessing the potential effect of magnitude on the maximum distance from the fault at which we observe ruptures, as well as diversity in azimuthal behavior.

The magnitude dependence in the models for individual events and for our general model is captured in parameter β, the expected average displacement measured at the primary fault. This parameter separates the Ridgecrest foreshock from the other events distinctly. For the other, M_W 7.1 to 7.3 events, the average displacements reflect variability that exceeds the expected differences as a function of magnitude within this narrow magnitude range, making the events indistinguishable from each other. An important implicit assumption in our model is that the event assessed has an observable surface rupture. The likelihood of an event having a surface rupture, which we do not account for, depends on event magnitude (e.g. Wells and Coppersmith, 1993), and is accounted for in models that consider hazard for a fault over multiple events (e.g. Petersen et al., 2011). Because our models are built to consider single events, we do not include a rate parameter that accounts for the frequency distribution of large events on a fault or its slip rate either (e.g. Petersen et al., 2011). Note that our model produces higher probabilities of observing a rupture (Equation 2) than previous models accounting for distributed ruptures (Petersen et al., 2011). These differences largely stem from the use of different input data.

Sources of uncertainty

Proper identification of the principal rupture trace is fundamental for the appropriate application of our model. The assumption of $S_0 << S_{max}$ in this model, required to obtain the expression in equation 7, underscores that our model is not appropriate to deduce the probability of large slip on a distributed rupture. This is a minor limitation in the sense that, a second rupture hosting a large slip is likely to be identified as an additional principal fault trace. Examples of this kind of categorization exist for the Ridgecrest mainshock and the El Mayor-Cucapah events (see figure 8 in the appendix), where multiple, parallel ruptures are classified as principal fault traces. Note that our model is not conditioned on prior knowledge of whether a fault exists or not (i.e. the model does not account for a site-specific understanding of the presence or absence, and age, of minor faults or shears).

Even when the principal rupture trace has been properly localized, there remains a small knee in the curve of $P(S > S_0)$ in the very near-fault region, inherited from parameter x_{fr} in the expression that describes the distribution of rupture density (equation 2). Parameter x_{fr} captures the uncertainty in the location of this primary rupture trace and is on the order of a few meters for the events with high-resolution maps we use in this study. The uncertainty in the fault location is an important parameter to consider in fault hazard assessments (e.g. Chen and Petersen, 2019; Scott et al., 2023).

We expect that the uncertainty in the principal fault trace location for faults without recent surface ruptures should be, at a minimum, comparable to the values of x_{fr} deduced from these datasets. Thus, we consider x_{fr} a useful parameter to incorporate into our model, as it results in a more conservative, wider zone of, high $P(S > S_0)$ near the fault. More conservative approaches to the error in the fault trace are given in Petersen et al. (2011) and Scott et al. (2023).

The Landers, Hector Mine, Ridgecrest, and El Mayor-Cucapah earthquakes show similar rupture distributions. The slopes (γ) or scaling exponents of rupture density that yield the probability of finding a rupture at a given distance from the fault overlap within error (Figure 2), though the exponents for the Ridgecrest foreshock and mainshock are comparatively lower than those for the other events. We suspect the gentler slope of the Ridgecrest events partly results from the inclusion of far-field features mapped as simplified lines based on geodetic observations, and from the more thorough far-field coverage during the field mapping. The variation of rupture densities at distances beyond 3 kilometers away from the main rupture likely results from variable mapping extent (e.g. far-field coverage is not complete for each event). Incomplete far field map coverage is accounted for in our uncertainties and reflected in the increase in uncertainty in our model with fault-perpendicular distance seen in Figure 7.

An important consideration regarding our model uncertainties is that the posterior distributions shown in Figures 2 and 3 only represent how well the models (equations 2 and 3) fit the spatial distributions of rupture density and average displacement. These distributions omit the epistemic uncertainty carried by these rupture maps and displacement measurements, which is associated with variability in mapping completeness throughout, as well as in individual mapper decisions when deciding where to place ruptures. The displacement distributions are also affected by the individual location errors for each displacement measurement. We expect larger location errors in the displacement measurements from the Landers and Hector Mine events, which predate the relaxation of selective availability for GPS locations.

Recommendations for future data collection

The epistemic uncertainties in these models could be largely mitigated through the data collection process in future surface-rupturing earthquakes. In the case of the rupture distributions, even coverage of the area surrounding the fault should largely reduce the far-field variability in the distributions and help establish whether a relationship between the location of the furthest rupture observed is magnitude-dependent. For the displacements, more careful documentation of the complete displacement range within the fault zone, without bias toward larger displacements, is necessary. This could be achieved through even sampling of displacement measurements along the principal rupture zones. In addition, careful documentation of the direction of displacement and separation of horizontal and vertical components would enable an expansion of this model to include displacement direction, an important component of assessing rupture hazard to engineered structures.

The characteristics of the events considered in this study make our model suitable for application to other faults in immature fault zones (<25 km of cumulative displacement) where large amounts of distributed deformation are expected, and in landscapes dominated by extensive sediment cover. Our framework may not be appropriate for more mature fault zones with a higher degree of strain localization (Dolan and Haravitch, 2014). Because the bulk of the surface ruptures we analyze occurred in sediment, the application of this model for events predominantly in bedrock remains to be tested. Last, events with substantial blind faulting may cause largely different distributed deformation patterns at the surface (e.g. Koehler et al., (2021), where a continuous, primary rupture trace cannot be defined, a requirement for the model proposed here.

Preliminary model implementation recommendations

In this contribution, we present a framework for how a distributed displacement model may approach the problems of distributed rupture density and displacement exceedance along strike-slip faults. In this section, we provide a set of preliminary guidelines to inform how practitioners and other users should consider the implementation of this framework to sample sites. This is a very general approach that does not take into account the peculiarities of specific structures (e.g. Valentini et al., 2021), only considering the dimensions and orientation of the site. From a hazard assessment perspective, we are interested in any scenario that includes at least one rupture hosting a displacement exceeding a threshold S_0 within the dimensions (A) of the site. The probability of this event is given by:

$$P_{site}(x, M_W, A) = 1 - \prod_{A} P(S < S_O | x, M_W, \delta a) \tag{11}$$

For simplicity, equation 11 assumes that the solutions for $P(S < S_O)$ are independent of each other for each area δa ($1m^2$ throughout this study). This is an assumption we made for the ruptures and the displacements in the rupture-perpendicular direction when fitting their spatial distributions. We now make this assumption in the rupture-parallel direction as well. Consulting projects will often involve sites with footprints in the 50-200 m^2 range. We apply equation 11 to the simple case of a 1 by 50 m long site parallel to a fault, located at 10 m from it in the fault-orthogonal direction. For this site, $P_{site}(x, M_W, A) = 0.39$, for a M_W 7 event and a displacement threshold S_0=0.1 m. Sites with dimensions exceeding 1 m in the fault-perpendicular direction may require accounting for the dependence of $P(S > S_0)$ on x, especially in the very near field of the fault.

Conclusions

Using detailed rupture maps from the Ridgecrest, Landers, Hector Mine, and El Mayor-Cucapah earthquakes in southern California and northern Mexico, we develop a framework for PFDHA that estimates the probability per unit area of finding a rupture with a displacement exceeding a threshold S_0, located at a given distance away from a principal fault trace. This model may be best applied to assess rupture hazard for a site in the near-field region (<3 km) of immature strike-slip faults (<25 km of cumulative displacement) where widespread distributed fault ruptures are expected, such as in the Eastern California Shear Zone or the Walker Lake Belt of the western United States.

References

1. S Baize, S Amoroso, N Belić, L Benedetti, P Boncio, M Budić, F R Cinti, M Henriquet, P Jamšek Rupnik, B Kordić, S Markušić, L Minarelli, D Pantosti, S Pucci, M Špelić, A Testa, S Valkaniotis, M Vukovski, J Atanackov, J Barbača, M Bavec, R Brajkovič, V Brčić, M Caciagli, B Celarc, R Civico, P M De Martini, R Filjak, F Iezzi, A Moulin, T Kurečić, M Métois, R Nappi, A Novak, M Novak, B Pace, D Palenik, T Ricci, Environmental effects and seismogenic source characterization of the December 2020 earthquake sequence near Petrinja, Croatia, Geophysical Journal International, Volume 230, Issue 2, August 2022, Pages 1394–1418, https://doi.org/10.1093/gji/ggac123

2. Chen, T., Akciz, S. O., Hudnut, K. W., Zhang, D. Z., & Stock, J. M. (2015). Fault-Slip Distribution of the 1999 M w 7.1 Hector Mine Earthquake, California, Estimated from Postearthquake Airborne LiDAR Data. Bulletin of the Seismological Society of America, 105(2A), 776-790.

3. Chen, R., & Petersen, M. D. (2019). Improved implementation of rupture location uncertainty in fault displacement hazard assessment. Bulletin of the Seismological Society of America, 109(5), 2132-2137.

4. R. Civico, S. Pucci, F. Villani, L. Pizzimenti, P. M. De Martini, R. Nappi & the Open EMERGEO Working Group (2018) Surface ruptures following the 30 October 2016 Mw 6.5 Norcia earthquake, central Italy, Journal of Maps, 14:2, 151-160, DOI: 10.1080/17445647.2018.1441756

5. Dolan, J. F., & Haravitch, B. D. (2014). How well do surface slip measurements track slip at depth in large strike-slip earthquakes? The importance of fault structural maturity in controlling on-fault slip versus off-fault surface deformation. Earth and Planetary Science Letters, 388, 38-47.

6. DuRoss, C. B., Gold, R. D., Dawson, T. E., Scharer, K. M., Kendrick, K. J., Akciz, S. O., ... & Zinke, R. (2020). Surface displacement distributions for the July 2019 Ridgecrest, California, earthquake ruptures. Bulletin of the Seismological Society of America, 110(4), 1400-1418.

7. Fletcher, J. M., Teran, O. J., Rockwell, T. K., Oskin, M. E., Hudnut, K. W., Mueller, K. J., ... & González-García, J. (2014). Assembly of a large earthquake from a complex fault system: Surface rupture kinematics of the 4 April 2010 El Mayor–Cucapah (Mexico) Mw 7.2 earthquake. Geosphere, 10(4), 797-827.

8. Hudnut, K. W., Borsa, A., Glennie, C., & Minster, J. B. (2002). High-resolution topography along surface rupture of the 16 October 1999 Hector Mine, California, earthquake (M w 7.1) from airborne laser swath mapping. Bulletin of the Seismological Society of America, 92(4), 1570-1576.

9. Hudnut, K. W., Brooks, B. A., Scharer, K., Hernandez, J. L., Dawson, T. E., Oskin, M. E., ... & Sorhus, S. (2020). Airborne lidar and electro-optical imagery along surface ruptures of the 2019 Ridgecrest earthquake sequence, southern California. Seismological Research Letters, 91(4), 2096-2107.

10. Koehler, R. D., Dee, S., Elliott, A., Hatem, A., Pickering, A., Pierce, I., & Seitz, G. (2021). Field response and surface-rupture characteristics of the 2020 M 6.5 Monte Cristo range earthquake, Central Walker Lane, Nevada. Seismological Research Letters, 92(2A), 823-839.

11. Lazarte, C. A., Bray, J. D., Johnson, A. M., & Lemmer, R. E. (1994). Surface breakage of the 1992 Landers earthquake and its effects on structures. Bulletin of the Seismological Society of America, 84(3), 547-561.

12. Mattioli, G. S., Phillips, D. A., Hodgkinson, K. M., Walls, C., Mencin, D. J., Bartel, B. A., ... & Zaino, A. (2020). The GAGE data and field response to the 2019 Ridgecrest earthquake sequence. Seismological Research Letters, 91(4), 2075-2086.

13. Milliner, C. W., Dolan, J. F., Hollingsworth, J., Leprince, S., Ayoub, F., & Sammis, C. G. (2015). Quantifying near-field and off-fault deformation patterns of the 1992 Mw 7.3 Landers earthquake. Geochemistry, Geophysics, Geosystems, 16(5), 1577-1598.

14. Milliner, C. W. D., Dolan, J. F., Hollingsworth, J., Leprince, S., & Ayoub, F. (2016). Comparison of coseismic near-field and off-fault surface deformation patterns of the 1992 Mw 7.3 Landers and 1999 Mw 7.1 Hector Mine earthquakes: Implications for controls on the distribution of surface strain. Geophysical Research Letters, 43(19), 10-115.

15. Milliner, C., & Donnellan, A. (2020). Using daily observations from Planet Labs satellite imagery to separate the surface deformation between the 4 July Mw 6.4 foreshock and 5 July Mw 7.1 mainshock during the 2019 Ridgecrest earthquake sequence. Seismological Research Letters, 91(4), 1986-1997.

16. Moss, R. E. S., & Ross, Z. E. (2011). Probabilistic fault displacement hazard analysis for reverse faults. Bulletin of the Seismological Society of America, 101(4), 1542-1553.

17. Nurminen, F., Boncio, P., Visini, F., Pace, B., Valentini, A., Baize, S., & Scotti, O. (2020). Probability of occurrence and displacement regression of distributed surface rupturing for reverse earthquakes. Frontiers in Earth Science, 8, 581605.

18. Petersen, M. D., Dawson, T. E., Chen, R., Cao, T., Wills, C. J., Schwartz, D. P., & Frankel, A. D. (2011). Fault displacement hazard for strike-slip faults. Bulletin of the Seismological Society of America, 101(2), 805-825.

19. Ponti, D. J., Blair, J. L., Rosa, C. M., Thomas, K., Pickering, A. J., Akciz, S., ... & Zinke, R. (2020). Documentation of surface fault rupture and ground-deformation features produced by the 4 and 5 July 2019 Mw 6.4 and Mw 7.1 Ridgecrest earthquake sequence. Seismological Research Letters, 91(5), 2942-2959.

20. Rodriguez Padilla, A. M., Quintana, M. A., Prado, R. M., Aguilar, B. J., Shea, T. A., Oskin, M. E., & Garcia, L. (2022a). Near-Field High-Resolution Maps of the Ridgecrest Earthquakes from Aerial Imagery. Seismological Society of America, 93(1), 494-499.

21. Rodriguez Padilla, A. M., Oskin, M. E., Milliner, C. W., & Plesch, A. (2022b). Accrual of widespread rock damage from the 2019 Ridgecrest earthquakes. Nature Geoscience, 15(3), 222-226.

22. Sarmiento, A., Madugo, D., Bozorgnia, Y., Shen, A., Mazzoni, S., Lavrentiadis, G., Dawson, T., Madugo, C., Kottke, A., Thompson, S., Baize, S., Milliner, C., Nurminen, F., Boncio, P., and Visini, F. (2021). Fault Displacement Hazard Initiative Database, UCLA B. John Garrick Institute for the Risk Sciences, Report GIRS-2021-08, doi: 10.34948/N36P48.

23. Sieh, K., Jones, L., Hauksson, E., Hudnut, K., Eberhart-Phillips, D., Heaton, T., ... & Zachariasen, J. (1993). Near-field investigations of the Landers earthquake sequence, April to July 1992. Science, 260(5105), 171-176.

24. Chelsea Scott, Rachel Adam, Ramon Arrowsmith, Christopher Madugo, Joseph Powell, John Ford, Brian Gray, Rich Koehler, Stephen Thompson, Alexandra Sarmiento, Timothy Dawson, Albert Kottke, Elaine Young, Alana Williams, Ozgar Kozaci, Michael Oskin, Reed Burgette, Ashley Streig, Gordon Seitz, William Page, Curtis Badin, Lorraine Carnes, Jacqueline Giblin, James McNeil, Jenna Graham, Daniel Chupik and Sean Ingersoll, Evaluating How Well Active Fault Mapping Predicts Earthquake Surface Rupture Locations, Geosphere, 2023.

25. Takao, M., J. Tsuchiyama, T. Annaka, and T. Kurita (2013). Application of probabilistic fault displacement hazard analysis in Japan, J. Jpn. Assoc. Earthq. Eng. 13, 17–36, doi: 10.5610/jaee.13.17.

26. Teran, O. J., Fletcher, J. M., Oskin, M. E., Rockwell, T. K., Hudnut, K. W., Spelz, R. M., ... & Morelan, A. E. (2015). Geologic and structural controls on rupture zone fabric: A field-based study of the 2010 Mw 7.2 El Mayor–Cucapah earthquake surface rupture. Geosphere, 11(3), 899-920.

27. Treiman, J. A., Kendrick, K. J., Bryant, W. A., Rockwell, T. K., & McGill, S. F. (2002). Primary surface rupture associated with the M w 7.1 16 October 1999 Hector mine earthquake, San Bernardino County, California. Bulletin of the Seismological Society of America, 92(4), 1171-1191.

28. Valentini, A., Fukushima, Y., Contri, P., Ono, M., Sakai, T., Thompson, S. C., ... & Youngs, R. R. (2021). Probabilistic fault displacement hazard assessment (PFDHA) for nuclear installations according to IAEA safety standards. Bulletin of the Seismological Society of America, 111(5), 2661-2672.

29. Wang, Y., & Goulet, C. (2021). Validation of fault displacements from dynamic rupture simulations against the observations from the 1992 landers earthquake. Bulletin of the Seismological Society of America, 111(5), 2574-2594.

30. Wells, D. L., & Coppersmith, K. J. (1993). Likelihood of surface rupture as a function of magnitude. Seismological Research Letters, 64(1), 54.

31. Wells, D. L., & Coppersmith, K. J. (1994). New empirical relationships among magnitude, rupture length, rupture width, rupture area, and surface displacement. Bulletin of the seismological Society of America, 84(4), 974-1002.

32. Xu, X., Sandwell, D. T., & Smith-Konter, B. (2020). Coseismic displacements and surface ruptures from Sentinel-1 InSAR: 2019 Ridgecrest earthquakes. Seismological Research Letters, 91(4), 1979-1985.

33. Youngs, R. R., Arabasz, W. J., Anderson, R. E., Ramelli, A. R., Ake, J. P., Slemmons, D. B., ... & Toro, G. R. (2003). A methodology for probabilistic fault displacement hazard analysis (PFDHA). Earthquake spectra, 19(1), 191-219.

Parameter	Landers	Hector Mine	El Mayor-Cucapah	Ridgecrest (foreshock)	Ridgecrest (mainshock)	General model
ν_o	0.15	0.12	0.12	0.31	0.20	0.13
x_{fr} (meters)	7.0	5.7	7.5	1.3	2.0	6.7
γ	1.29	1.28	1.11	0.88	0.94	1.19
β (meters)	2.1	4.2	3.1	1.0	2.9	$\beta(M_W)$
n	0.37	0.40	0.42	0.51	0.36	0.41

Table 1. Distribution of best-fit parameters for each event and the general model in equation 8.

536 # Appendix

537 ## Supplementary figures

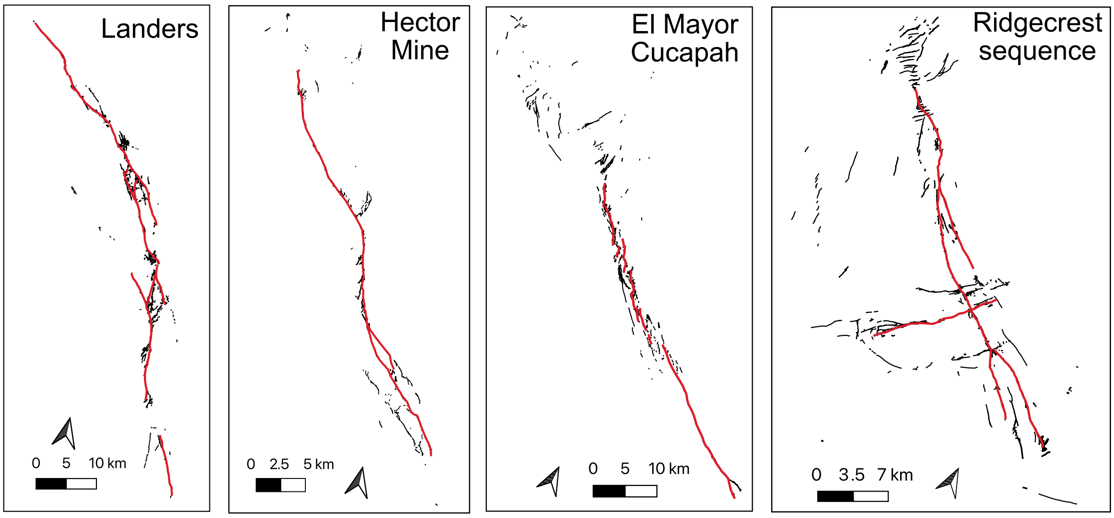

Figure 8: Distributed ruptures (black) and simplified principal rupture trace (red) for each event considered in this study.

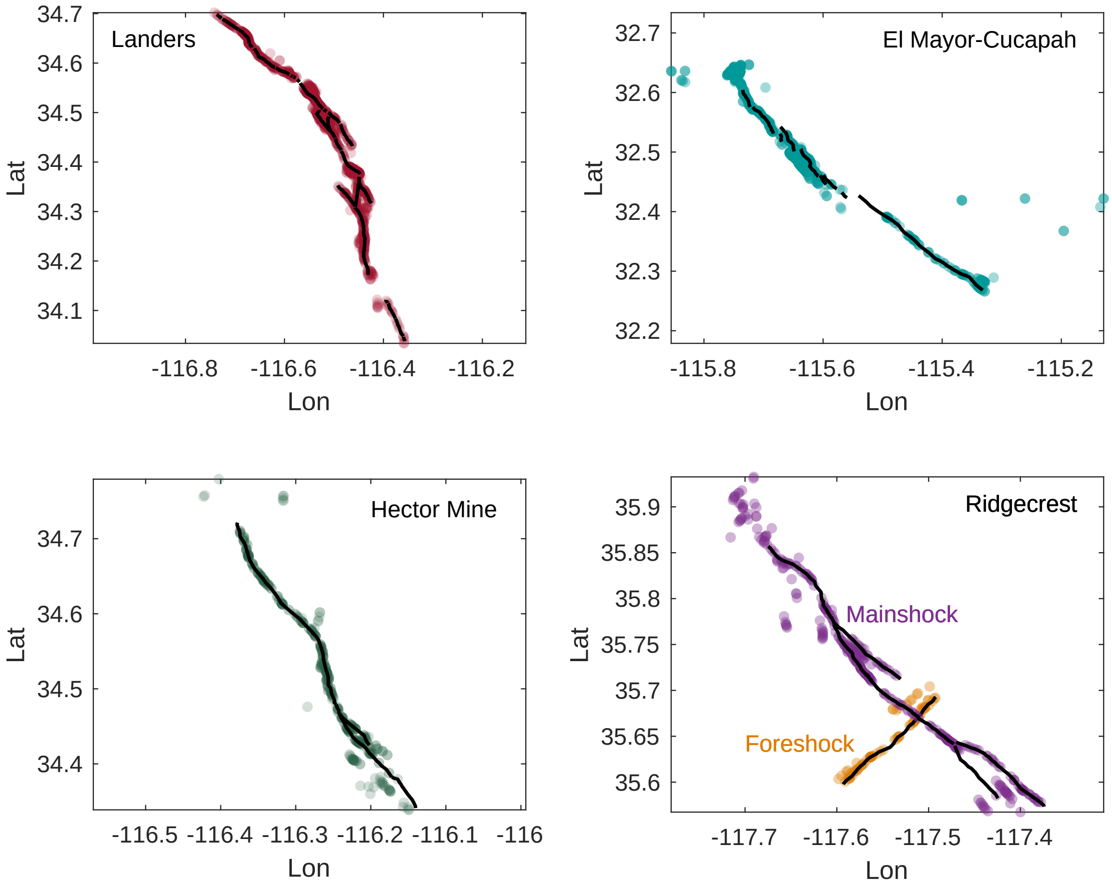

Figure 9: Displacement data from the Landers (red), Hector Mine (green), El Mayor-Cucapah (teal), and Ridgecrest earthquakes (foreshock in orange and mainshock in purple) plotted over the principal rupture trace of each event. The displacement data is sourced from the Fault Displacement Hazard Initiative database (Sarmiento et al., 2021) and we only consider measurements collected in the field. The principal rupture traces are roughly simplified from the ruptures classified as primary in the FDHI database (see figure 8) in the appendix.

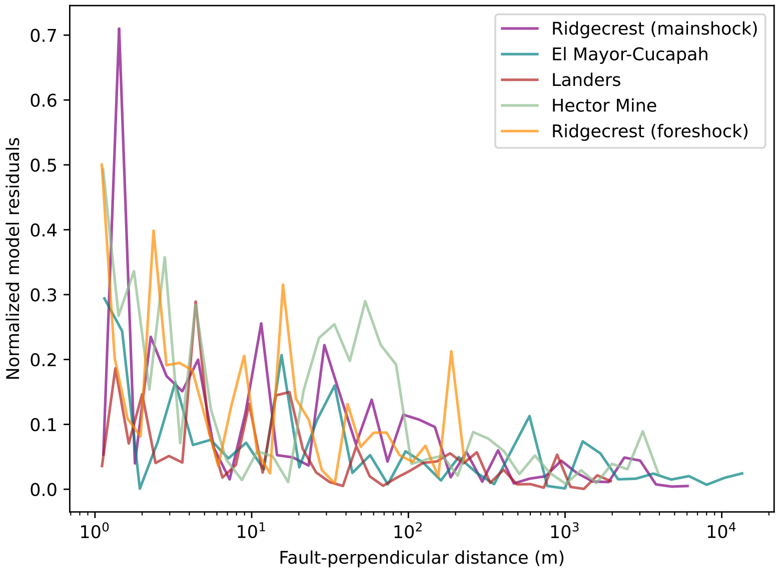

Figure 10: Model residuals from the best fits of equation 3 to the field displacement data in the FDHI database for each event (Figure 3). The residuals are normalized by the value of β for each event to account for the magnitude-dependence of displacement.

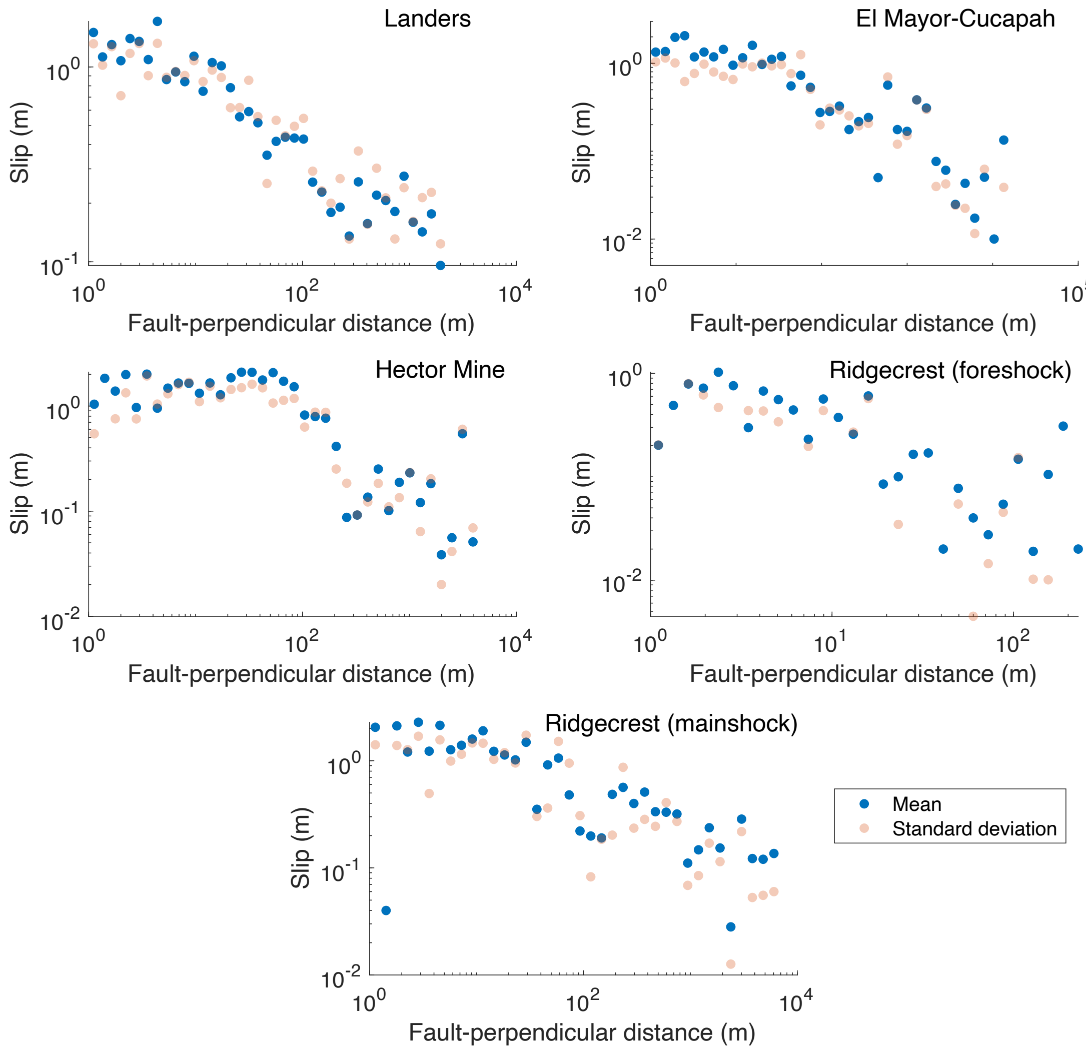

Figure 11: Mean (blue) and standard deviation (pink) of slip with fault-perpendicular distance for the Landers, Hector Mine, El Mayor-Cucapah, and Ridgecrest earthquakes. The consistent correlation of the mean and the standard deviation suggests the displacements are exponentially distributed within each distance bin.

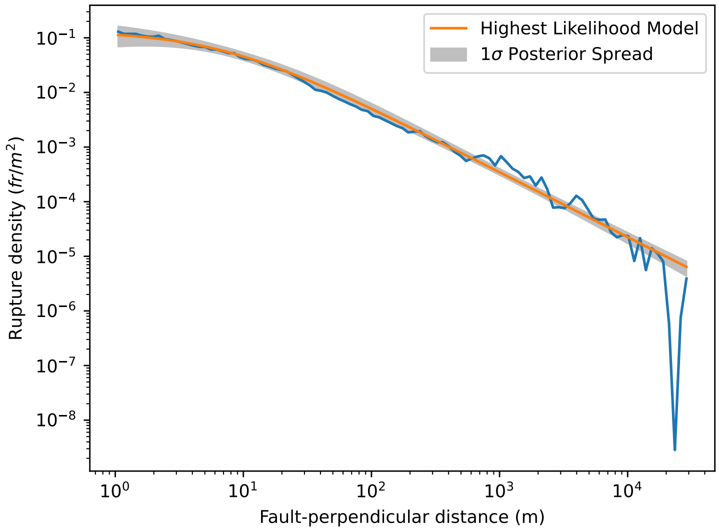

Figure 12: General model for the decay of rupture density with fault-perpendicular distance generated from combining the distributed rupture maps from the Landers, Hector Mine, El Mayor-Cucapah, and Ridgecrest earthquakes.

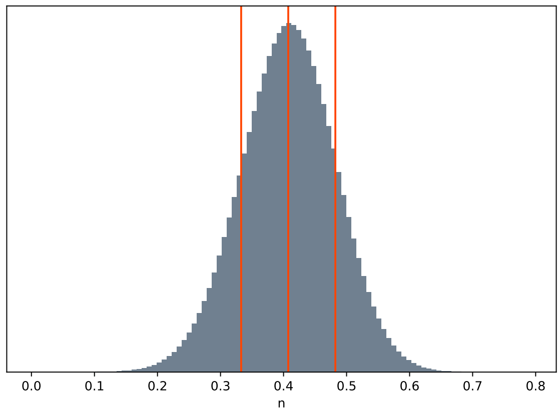

Figure 13: Concatenated posteriors for n in equations 3 and 8 from the Landers, Ridgecrest mainshock, and El Mayor-Cucapah event. Note that n is roughly normally distributed. The vertical red lines indicate the mean and data within one standard deviation of the mean.

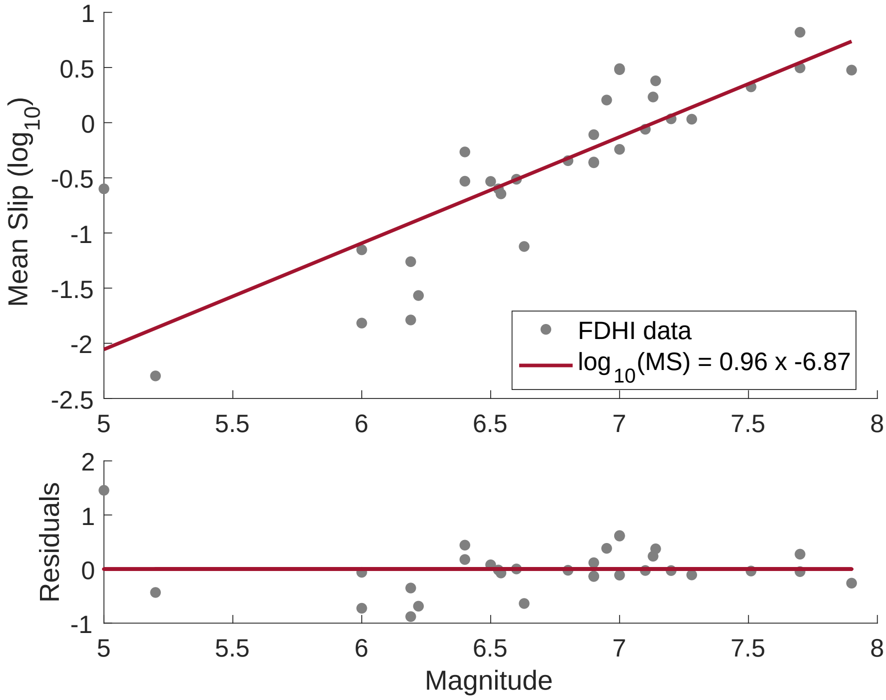

Figure 14: Top: Scaling of mean slip in meters with event magnitude for the strike-slip events in the FDHI database (Sarmiento et al., 2021). The best fit to the data using a least-squares approach is shown in the solid maroon line. Bottom: Model residuals.

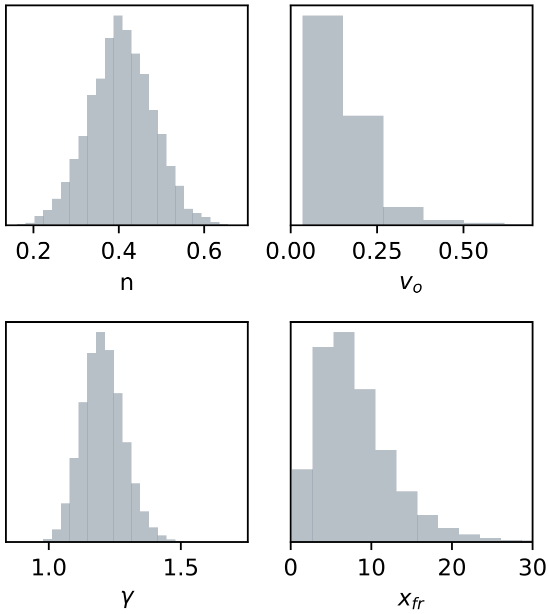

Figure 15: Distribution of parameters from equation 8. ν_o, x_{fr}, and γ are sampled from the posterior distributions of the fits in supplementary figure 12. n is sampled from a normal distribution where the mean and standard deviation of are calculated from the posterior distributions of the events well described by the displacement model in equation 3 (figure 13.)

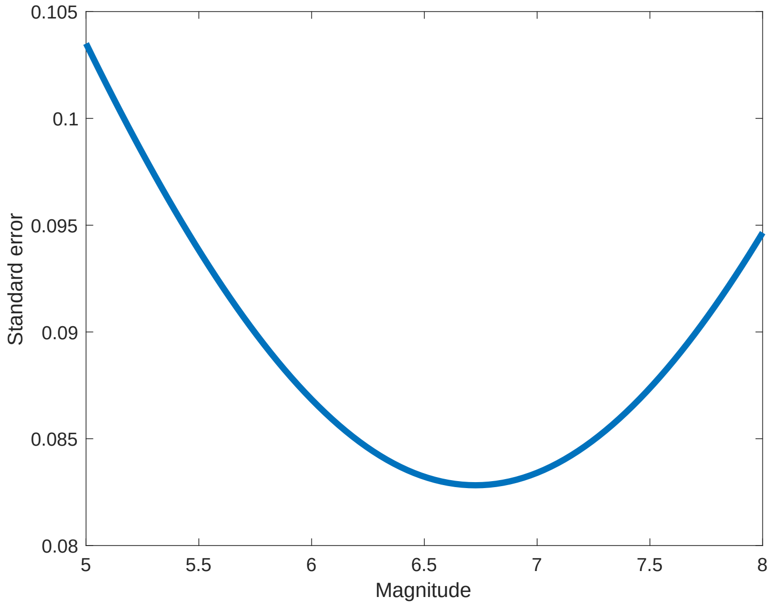

Figure 16: Standard error as a function of magnitude for the general model based on the standard error of the regression in figure 14.

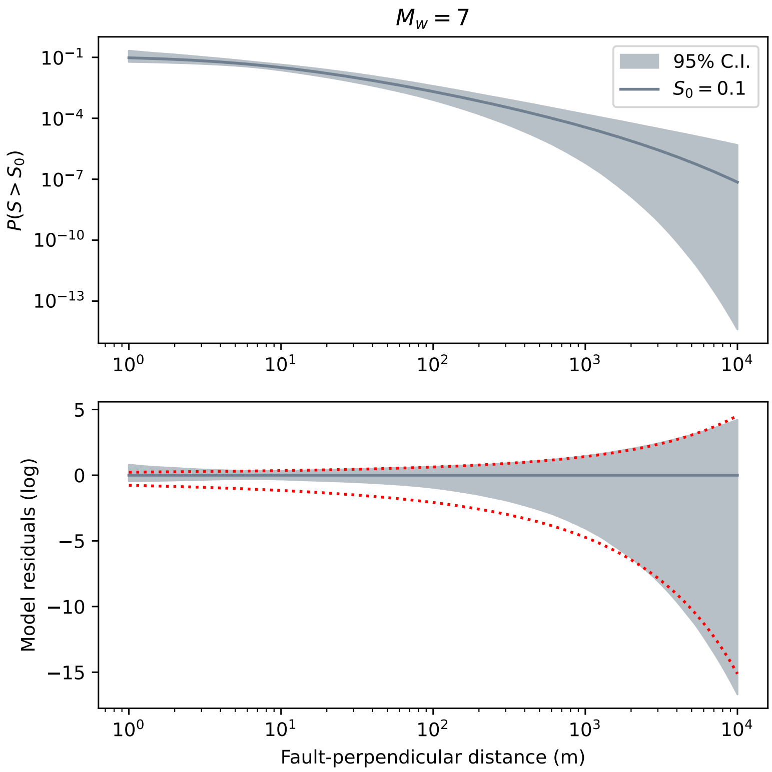

Figure 17: Top: PFDHA model expressing the probability of finding a rupture hosting a displacement that exceeds threshold $S_0 = 0.1$ m for a surface-rupturing strike-slip earthquake of M_W 7. The model is generated using equation 8. The shading represents the 95% confidence intervals. The solid line represents the best-fit model. Bottom: Model residuals. The dotted red line represents the fit of equation 10 logarithm of the residuals.

Supplementary methods

We build on the method in Rodriguez Padilla et al. (2022b) to estimate the decay of rupture density with fault-perpendicular distance for each event. We begin by discretizing every rupture into 1m spaced points, to minimize the effect of mapper bias in rupture continuity. Next, we measure the distance between each point and the nearest point on the main rupture. The principal rupture is simplified for each event from the cracks defined as primary in the FDHI rupture database (supplementary figure 8). We then log bin the distances into 100 bins, from 0 to the furthest rupture from the main rupture, and count the number of rupture segments per bin. Last, we normalize each bin by its size, and the entire decay by the total length of the principal fault. This produces the decays shown in Figure 2.

We fit each decay with an affine-invariant ensemble sampler for Markov Chain Monte Carlo (Goodman and Weare, 2010; Foreman-Mackay et al., 2013) to estimate the maximum likelihood parameters for equation 2. As priors, we use uniformly distributed values of ν_o= (0,3), x_{fr}= (0, 100) meters, and γ = (0, 3). We assume that the error of $\nu(x)$ in each bin is Poisson-distributed, following the method of Powers and Jordan (2010). We employ an ensemble of 200 walkers, which run for 100,000 iterations, following a 10,000-iteration burn-in period.

We follow a similar approach to estimate the decay of average displacement with fault-perpendicular distance. We take the displacements from the FDHI database for each event and measure their distance to the principal rupture trace (supplementary figure 8). We then log-bin the distances into 40 bins, from 0 to the furthest rupture from the main rupture, and calculate the average displacement per bin. Note we use a smaller number of bins for the displacement data than the rupture locations (Figure 1) because of the smaller number of displacement measurements (Figure 9 in the appendix). This binning produces the decays shown in Figure 3. We fit each decay with an affine-invariant ensemble sampler for Markov Chain Monte Carlo (Goodman and Weare, 2010; Foreman-Mackay et al., 2013) to estimate the maximum likelihood parameters for equation 3. As priors, we use uniformly distributed values of β= (0,15) meters and n=(0,3). We employ an ensemble of 200 walkers, which run for 100,000 iterations, following a 10,000-iteration burn-in period. Note that we fix $x_S = 1$ meter in equation 3 because this provides a better model fit than letting x_S be a free parameter that is fit with the ensemble sampler for Markov Chain Monte Carlo and contributes to reducing uncertainty in the model fits. We also tested values of $x_S = 10$ meters, with worse residuals, thus the choice of $x_S = 1$ meter.

Supplementary references

1. Foreman-Mackey, D., Hogg, D. W., Lang, D., & Goodman, J. (2013). emcee: the MCMC hammer. Publications of the Astronomical Society of the Pacific, 125(925), 306.

2. Goodman, J., & Weare, J. (2010). Ensemble samplers with affine invariance. Communications in applied mathematics and computational science, 5(1), 65-80.

3. Powers, P. M., & Jordan, T. H. (2010). Distribution of seismicity across strike-slip faults in California. Journal of Geophysical Research: Solid Earth, 115(B5).